IEEE Transactions on Quantum Engineering

Received 8 May 2023; revised 24 August 2023; accepted 9 October 2023; date of publication 16 October 2023; date of current version 6 November 2023.

Digital Object Identifier 10.1109/TQE.2023.3324841

Optimal Control of the Operating Regime of a Single-Electron Double Quantum Dot

V. REIHER[1,2] AND Y. BÉRUBÉ-LAUZIÈRE[1,2]

[1]Département de Génie Électrique et de Génie Informatique, Université de Sherbrooke, Sherbrooke, QC J1K 2R1, Canada
[2]Institut quantique, Université de Sherbrooke, Sherbrooke, QC J1K 2R1, Canada

Corresponding author: Y. Bérubé-Lauzière (e-mail: yves.berube-lauziere@usherbrooke.ca).

The work of V. Reiher was supported in part by ES-D—Bourses d'études supérieures au doctorat from the Conseil de recherche en sciences naturelles et en génie du Canada, in part by B1X—Bourses de maîtrise en recherche fromi the Fonds de recherche du Québec Nature et technologies, and in part by Bourse VoiceAge pour l'excellence académique aux études supérieures from the Université de Sherbrooke. The work of Y. Bérubé-Lauzière was supported by the Canada First Research Excellence Fund and Institut quantique at Université de Sherbrooke.

ABSTRACT The double-quantum-dot device benefits from the advantages of both the spin and charge qubits, while offering ways to mitigate their drawbacks. Careful gate voltage modulation can grant greater spinlike or chargelike dynamics to the device, yielding long coherence times with the former and high electrical susceptibility with the latter for electrically driven spin rotations or coherent interactions with microwave photons. As this architecture is a serious contender for the realization of a versatile physical qubit, improving its control is a critical step toward building a large-scale spin-based universal quantum computer. We show that optimal control pulses generated using the gradient ascent pulse engineering algorithm can yield higher fidelity operating regime transfers than can be achieved using linear methods.

INDEX TERMS Double quantum dot (DQD), gradient ascent pulse engineering (GRAPE), optimal control, quantum computing, quantum control.

I. INTRODUCTION

Ever since Loss and DiVincenzo's proposal to use the electron spin as the fundamental building block for quantum computing [1], important efforts have been devoted to the development of spin qubit architectures [2], [3], [4], [5]. The long coherence times of electron spins, which have reached the order of seconds in silicon [3], [6], [7], [8], as well as the existing fabrication infrastructure of the silicon industry, make them great candidates for physical qubit implementations. However, although high-fidelity initialization, manipulation, and readout of small numbers of spins isolated within quantum dots have been demonstrated [4], [9], [10], [11], [12], [13], the fabrication of 2-D arrays of interconnected spins, required for quantum information processing and error correction, remains an outstanding challenge [14], [15], [16].

One avenue to solving this challenge lies in using microwave photons in superconducting resonators to mediate long-range spin–spin interactions, as demonstrated for superconducting qubits [17], [18], [19]. Coherent interactions between single spins and microwave photons have already been shown using the large electric dipole of the electron charge state in a double quantum dot (DQD) through spin-charge hybridization [20], [21], [22]. Conversely, the increased electrical susceptibility of such a device can be used to drive spin state rotations via electric dipole spin resonance (EDSR) by quickly displacing the electron wave function in an oscillatory motion in a local transverse magnetic field gradient [23], [24], [25], [26]. In addition, gate voltages can be modulated to reshape the double-well potential and reach the single-dot regime, decoupling the spin and charge degrees of freedom and recovering long coherence times [20], [25].

The single-electron DQD, therefore, presents itself as a promising architecture for quantum computation, with two outstanding operating regimes.

1) A memory-mode regime wherein the electron is strongly localized in one of the two wells of the DQD due to a large interdot energy detuning. In this regime, the qubit dynamics approach that of a pure spin and are largely decoupled from environmental charge noise, recovering the long natural coherence times of electron spins in silicon.
2) A flopping-mode regime corresponding to a set of configurations wherein the electron charge state is delocalized across the two dots of the DQD. When the electron orbital and Zeeman energies approach resonance, this regime allows for fast manipulation of the electron spin

state via EDSR to realize one-qubit gates or reaching the strong coupling regime between the electron spin and a microwave photon for long-range interactions between distant spins or for dispersive measurement of the qubit state.

In the context of a quantum computation, such a device will be transferred many times between these operating regimes. It is, therefore, crucial that this transfer be made quickly and that it preserves maximal state fidelity in the *logical basis*. This is the problem dealt with in this article.

In recent years, significant efforts have been deployed to develop advanced control methods relying on optimal control theory (OCT) for a wide range of spin systems [27], [28], [29], [30], [31], [32], [33], [34]. While these schemes benefit from extreme versatility, control equations derived from the variational principle, an approach often referred to as "full OCT," are generally hard to solve analytically and expensive to solve numerically. In contrast, when the control objective is well defined, the existing open-loop optimal control algorithms, such as gradient ascent pulse engineering (GRAPE) [35], allow fast generation of optimal control signals, which have been used experimentally to manipulate physical qubits [36], [37], [38], [39]. These algorithms employ clever strategies to either reduce the computational cost of evaluating the gradient of the cost function or to reduce how many time evolutions are required for each iteration of the optimization loop, thus converging much faster. It will be demonstrated in this article that experimentally realistic control signals obtained using the GRAPE algorithm combined with pulse windowing and filtering provide faster and higher fidelity operating regime transfers than can be attained using standard linear approaches. This is achieved independently of the qubit's state and, therefore, does not require a priori knowledge of the qubit state, which is of prime importance in practice. For a brief reminder of the GRAPE algorithm, see Appendix C.

The rest of this article is organized as follows. Section II describes the model of the DQD device considered herein. The control objective used to optimize control pulses to alter the device's operating regime while preserving its logical state is formulated in Section III. Section IV provides the results obtained from the application of optimal control pulses to transfer between the different operating regimes of the system for various qubit states. Section V discusses considerations for the experimental implementation of the resulting optimal control pulses. Finally, Section VI concludes this article.

II. MODEL

The physical system consists of a gate-defined DQD in silicon (see Fig. 1), tuned to the single-electron regime, as described in [20]. The device is subjected to a strong homogeneous longitudinal magnetic field B_z and a weak transverse magnetic field gradient B_x. Gate voltages directly control the tunnel coupling t_c between the left and right dots as well

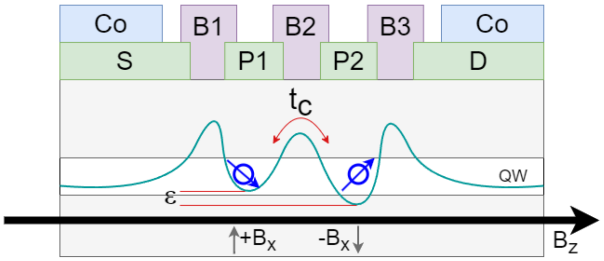

FIGURE 1. Schematic of the device under control. A single electron is trapped within a double-well potential. The device is influenced by an external magnetic field B_z, a local magnetic field gradient B_x generated by cobalt micromagnets, and voltages on the barrier (B) and plunger (P) gates controlling the detuning energy ϵ and tunnel coupling t_c. Figure adapted from [20] and [21].

as the energy detuning ϵ between the two dots. The DQD system Hamiltonian can be written as

$$H = \frac{1}{2}\left(\epsilon\tau_z + 2t_c\tau_x + g\mu_B B_z\sigma_z + g\mu_B B_x\sigma_x\tau_z\right) \tag{1}$$

where σ_α are the Pauli matrices for the spin degree of freedom with basis $\{|\uparrow\rangle, |\downarrow\rangle\}$ and τ_α are the Pauli matrices for the charge degree of freedom, in the left–right basis $\{|L\rangle, |R\rangle\}$, with $|L\rangle$ and $|R\rangle$ being the electron charge states corresponding to occupation in the left and right dots, respectively. The valley degree of freedom is neglected here, as recent measurements on similar devices have shown sufficiently large valley splittings [40]. The eigenstates of this four-level Hamiltonian are written as [20]

$$|0\rangle \approx |-,\downarrow\rangle \tag{2}$$

$$|1\rangle = \cos\frac{\phi}{2}|-,\uparrow\rangle + \sin\frac{\phi}{2}|+,\downarrow\rangle \tag{3}$$

$$|2\rangle = -\sin\frac{\phi}{2}|-,\uparrow\rangle + \cos\frac{\phi}{2}|+,\downarrow\rangle \tag{4}$$

$$|3\rangle \approx |+,\uparrow\rangle \tag{5}$$

where ϕ is the spin–orbit mixing angle. The symmetric and antisymmetric charge states are defined as

$$|+\rangle = \cos\frac{\theta}{2}|L\rangle + \sin\frac{\theta}{2}|R\rangle \tag{6}$$

$$|-\rangle = -\sin\frac{\theta}{2}|L\rangle + \cos\frac{\theta}{2}|R\rangle \tag{7}$$

where $\theta = \frac{\pi}{2} - \arctan\frac{\epsilon}{2t_c}$ is the orbital angle. For the purposes of the present work, the qubit is defined on the $|0\rangle \leftrightarrow |1\rangle$ transition. The spin–orbit mixing angle describes the spinlike or chargelike character of the qubit: it is readily seen from (2) and (3) that for $\phi = 0$, this transition forms a pure spin qubit, and that for $\phi = \pi$, this transition forms a pure charge qubit. The spin–orbit mixing angle is given by

$$\phi = \arctan\frac{g\mu_B B_x\cos\theta}{\Omega - g\mu_B B_z} \tag{8}$$

where $\Omega = \sqrt{\epsilon^2 + 4t_c^2}$ is the orbital energy. Here, we define the arctangent function on the $[0, \pi]$ interval due to the

IEEE Transactions on Quantum Engineering

definition of θ, which avoids undefined results for $\epsilon = 0$. Owing to the transverse magnetic field gradient, the electron dipole operator acquires off-diagonal elements, which couple $|-,\uparrow\rangle$ and $|+,\downarrow\rangle$ states, leading to anticrossings in the energy spectrum as the detuning energy ϵ varies [20].

In addition to coherent evolution according to its Hamiltonian, the DQD is, in general, subject to dephasing and relaxation in both the spin and charge subspaces. Direct spin relaxation is typically a very slow process [41] and is neglected in this work. Spin dephasing via hyperfine interactions and charge dephasing due to quasi-static charge noise in the device are stable processes with rates, which do not vary appreciably over the duration of a control sequence [42], [43]; they can, therefore, be approximated to constant rates. For the purpose of numerical simulation of decoherence processes in this work, the charge and spin dephasing rates are set to $\gamma_{\phi,c}/2\pi = 36$ MHz and $\gamma_{\phi,s}/2\pi = 1.2$ MHz, respectively, according to the literature [20], [21]. Finally, charge relaxation via emission of longitudinal acoustic (LA) phonons in the silicon lattice is the dominating process and is dependent on the control amplitudes ϵ and t_c via the orbital energy $\Omega \equiv \Omega(\epsilon, t_c)$. This rate has been set to a constant $\gamma_{1,c}/2\pi = 45$ MHz in this work, given the dynamical range considered for parameters ϵ and t_c, in an effort to reduce the computational complexity of the problem and avoid transcendental equations (see Appendix A). While this noise model for the device is only an approximation of the real processes that would be experimentally measured, an exact description of the decoherence channels for the DQD is outside the scope of this work; moreover, the difference between this approximated noise model and the real noise processes present in the device is not expected to appreciably impact the results presented below, as the control operation timescales considered here are very short relative to typical decoherence rates for this type of device.

To model the time evolution of the state system, as is customary, we combine the device Hamiltonian with decoherence operators to yield the Lindblad master equation [44], [45] of the system

$$\dot{\rho} = -\frac{i}{\hbar}[H, \rho] + \sum_i \gamma_i \left(L_i \rho L_i^\dagger - \frac{1}{2}\{L_i^\dagger L_i, \rho\} \right) \tag{9}$$

where ρ is the system's density matrix, $\{a, b\}$ is the anticommutator of operators a and b, and γ_i and L_i are the rates and associated operators for the decoherence channels relevant to this system, respectively

$$\gamma_1 = \gamma_{1,c}, \quad L_1 = \tau_- \tag{10}$$

$$\gamma_2 = \gamma_{\phi,c}, \quad L_2 = \tau_z \tag{11}$$

$$\gamma_3 = \gamma_{\phi,s}, \quad L_3 = \sigma_z. \tag{12}$$

These equations are used to generate optimal control signals through the GRAPE algorithm, as well as to simulate the state evolution under the effect of the control scheme and evaluate its performance.

III. CONTROL OBJECTIVE

As mentioned in the introduction, the aim is to transfer the qubit between an initial and final operating regimes while preserving the qubit's logical state. Each operating regime is defined by its spin–orbit mixing angle ϕ or equivalently by its orbital energy Ω and orbital angle θ. These parameters, in turn, define the required values for the interdot energy detuning ϵ and tunnel coupling t_c, which are the parameters that can be directly electrically controlled by the experimenter.

The control objective is, thus, to preserve the initial logical state while the qubit's operating regime changes. Of course, and this is the key point, as that regime changes, so does its Hamiltonian and eigenstates. It, therefore, follows that the total effect of the control on the qubit state must compensate for this change such that the final logical state (in the new eigenbasis) is the same as the initial logical state in the initial eigenbasis.

Let the initial qubit logical state be written in general form as

$$|\Psi_i\rangle = \alpha_i |0_i\rangle + \beta_i |1_i\rangle \tag{13}$$

where $|0_i\rangle$ and $|1_i\rangle$ are eigenstates of the DQD Hamiltonian in the initial operating regime. Using the initial and final Hamiltonian eigenbases as logical bases

$$\mathscr{L}_{i,f} = \left\{ |0_{i,f}\rangle, |1_{i,f}\rangle, |2_{i,f}\rangle, |3_{i,f}\rangle \right\} \tag{14}$$

the column vectors containing the coefficients of the initial and final logical qubit states that represent these states with respect to the initial and final eigenbases are written as

$$[\Psi_i]_{\mathscr{L}_i} = \begin{bmatrix} \alpha_i & \beta_i & 0 & 0 \end{bmatrix}^T \tag{15}$$

$$[\Psi_f]_{\mathscr{L}_f} = \begin{bmatrix} \alpha_f & \beta_f & \gamma_f & \delta_f \end{bmatrix}^T. \tag{16}$$

However, to preserve the qubit's logical state through the operating regime transfer, it is necessary that the total effect of the control in the logical basis be equal to the identity, i.e.,

$$[\Psi_f]_{\mathscr{L}_f} = \mathbb{1}_{\mathscr{L}_f \mathscr{L}_i} [\Psi_i]_{\mathscr{L}_i} = \begin{bmatrix} \alpha_i & \beta_i & 0 & 0 \end{bmatrix}^T \tag{17}$$

where $\mathbb{1}_{\mathscr{L}_f \mathscr{L}_i}$ is an identity matrix with ones on its diagonal. The coefficients of the logical qubit state in the initial eigenbasis are, therefore, preserved, and the population of the higher excited states is kept to $\gamma_f = \delta_f = 0$, protecting the quantum information encoded within the qubit state through the change of bases induced by the operating regime transfer.

Considering, instead, the effect of the control in the product basis of the DQD charge and spin states, henceforth referred to as the physical basis

$$\mathscr{P} = \{|L\rangle, |R\rangle\} \otimes \{|\downarrow\rangle, |\uparrow\rangle\} \tag{18}$$

the ideal evolution of the initial physical state to the final physical state in this basis, in the absence of decoherence, is written as

$$[\Psi_f]_{\mathscr{P}} = \mathbf{U}_{\mathscr{P}\mathscr{P}} [\Psi_i]_{\mathscr{P}} \tag{19}$$

where $\mathbf{U}_{\mathscr{P}\mathscr{P}}$ is the evolution operator expressed in the physical basis and obtained by the usual exponentiation of the integral of the Hamiltonian operator over the evolution time. The exact expression is not important here, as will be seen next; this is, however, the operator that must be synthesized via optimal control. Using the basis change matrix $\mathcal{P}_{\mathscr{P}\leftarrow\mathscr{L}_{i,f}}$ from the initial or final logical basis to the physical basis and the change of basis formula [46], the total effect of the operating regime transfer in the logical bases is given by

$$[\Psi_f]_{\mathscr{L}_f} = \mathcal{P}_{\mathscr{L}_f\leftarrow\mathscr{P}}\mathbf{U}_{\mathscr{P}\mathscr{P}}\mathcal{P}_{\mathscr{P}\leftarrow\mathscr{L}_i}[\Psi_i]_{\mathscr{L}_i}. \tag{20}$$

Recall that $\mathcal{P}_{\mathscr{P}\leftarrow\mathscr{L}_i}$ contains in its columns the coefficients of the basis vectors of $\mathscr{L}_i$ decomposed along the basis vectors of $\mathscr{P}$ (the notation in [46] is used here). Identification of (20) with (17) as a condition on the effect of the control yields

$$\mathbb{1}_{\mathscr{L}_f\mathscr{L}_i} = \mathcal{P}_{\mathscr{L}_f\leftarrow\mathscr{P}}\mathbf{U}_{\mathscr{P}\mathscr{P}}\mathcal{P}_{\mathscr{P}\leftarrow\mathscr{L}_i} \tag{21}$$

which, in turn, leads to an analytical expression for the target control operator

$$\mathbf{U}_{\mathscr{P}\mathscr{P}} = \mathcal{P}_{\mathscr{P}\leftarrow\mathscr{L}_f}\mathcal{P}_{\mathscr{L}_i\leftarrow\mathscr{P}}. \tag{22}$$

It is this operator toward which the optimization algorithm must converge.

The following time-dependent Hamiltonian is used as a starting point for optimization:

$$H(t) = \frac{1}{2}\left(\epsilon(t)\tau_z + 2t_c(t)\tau_x + g\mu_B B_z\sigma_z + g\mu_B B_x\sigma_x\tau_z\right) \tag{23}$$

along with the controls

$$\epsilon(t) = \epsilon_i + \frac{t}{T}(\epsilon_f - \epsilon_i) + u_\epsilon(t) \tag{24}$$

$$t_c(t) = t_{c_i} + \frac{t}{T}(t_{c_f} - t_{c_i}) + u_{t_c}(t) \tag{25}$$

where $\epsilon_{\{i,f\}}$ and $t_{c_{\{i,f\}}}$ are the initial and final detuning and tunnel coupling energies, respectively, and T is the control pulse duration. It is seen that each of these controls consists of a linearly ramped part (which is customarily used) plus an additional control term $u_\epsilon(t)$ or $u_{t_c}(t)$. These additional terms are, here, iteratively optimized using the GRAPE [35] algorithm, such that the operator representing the overall effect of the controls converges toward operator $\mathbf{U}$.

IV. NUMERICAL RESULTS

We now apply the GRAPE algorithm to generate optimal control fields $u_\epsilon(t)$ and $u_{t_c}(t)$. The system is initially set in the memory-mode spin-qubit configuration, corresponding to a strongly detuned double-well potential with $\epsilon = 40\ \mu$eV and $t_c = 10\ \mu$eV; the final target configuration is the flopping-mode regime with strong chargelike dynamics, defined as $\epsilon = 0\ \mu$eV and $t_c = 16\ \mu$eV. This symmetric configuration increases the spin-charge hybridization, yielding strong coupling of the electron spin to the electric field while keeping the added charge noise sensitivity to a minimum, as discussed in [20]. The static magnetic fields used are $g\mu_B B_x = 1.62\ \mu$eV and $g\mu_B B_z = 24\ \mu$eV. Fig. 2 shows the operating regime transfer process fidelity; that is, how closely the effect of the optimal control fields recreates the target control operator $\mathbf{U}$. Owing to uncontrollable Hamiltonian evolution of the spin degree of freedom, the operator fidelity obtained with optimal control pulses exhibits an oscillating behavior with regard to the duration of the control sequence, and it is expected that high-fidelity operating regime transfers can only be performed for some precise pulse durations.

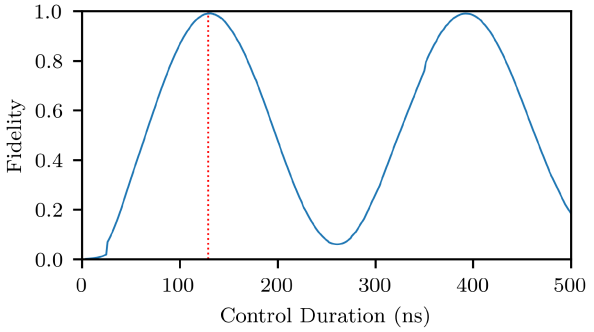

FIGURE 2. Optimized control operator fidelity as a function of control pulse duration T. This particular simulation aims to design the pulse required to transfer the device from the spin qubit configuration to the flopping-mode configuration. Operator fidelity greater than 99% is first reached for a 129-ns control pulse duration (vertical dotted line).

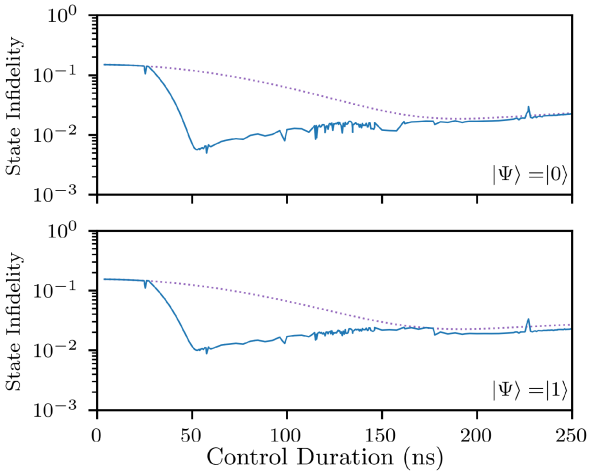

FIGURE 3. State infidelity for operating regime transfers of qubit eigenstates (top) $|0\rangle$ and (bottom) $|1\rangle$, from the memory-mode configuration to the flopping-mode configuration, as a function of control pulse duration T. In both the cases, peak controlled fidelity greater than 99% is reached for a 52.8-ns pulse duration (solid line), whereas linear ramping of the electrical parameters (dotted line) reaches a peak fidelity of 97.7% for 193-ns pulses.

A. QUBIT EIGENSTATE TRANSFER

When the qubit state is initially prepared in an eigenstate ($|\Psi_i\rangle = |0_i\rangle$ or $|\Psi_i\rangle = |1_i\rangle$), it is found that the optimal control pulses reach high-fidelity operating regime transfers much faster than regular linear ramping of the electrical parameters ϵ and t_c (see Fig. 3). Using GRAPE-designed control pulses represents a 72% reduction in the time required to perform this operating regime transfer while also allowing higher fidelity preservation of the qubit state.

IEEE Transactions on Quantum Engineering

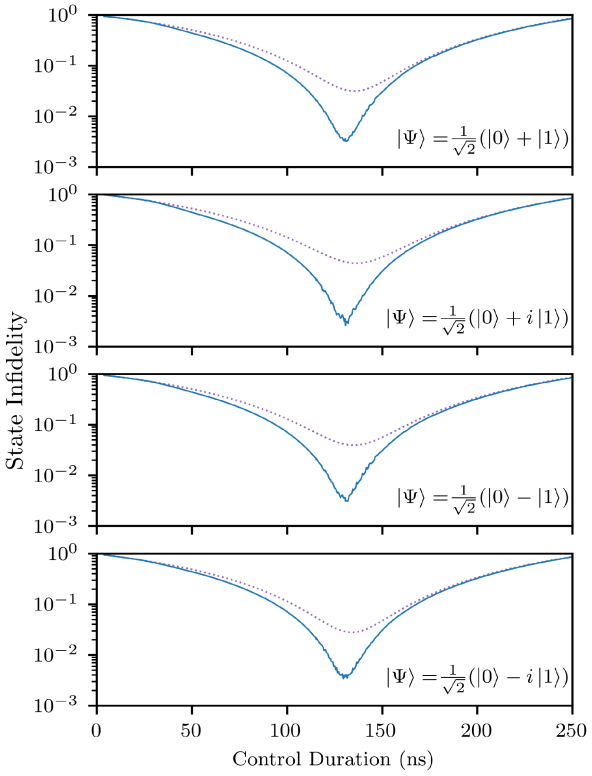

FIGURE 4. State infidelity for operating regime transfers of qubit equator states from the memory-mode configuration to the flopping-mode configuration, as a function of control pulse duration T. A 134.6-ns optimal control pulse (solid line) reaches a fidelity greater than 99%, whereas the linear ramp (dotted line) reaches a maximal fidelity of 96.9%.

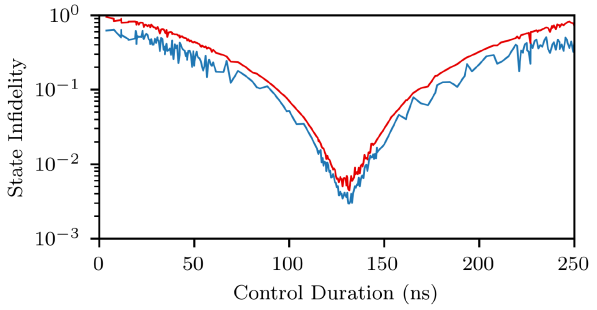

FIGURE 5. Average state infidelity (in blue) for operating regime transfers of randomly generated qubit states from the memory-mode configuration to the flopping-mode configuration, as a function of control pulse duration T. The maximal state infidelity (in red) found for each pulse duration shows that a 134.6-ns optimal control pulse reaches a fidelity greater than 99% in all the cases.

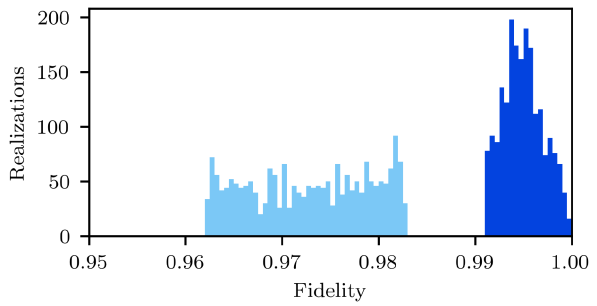

FIGURE 6. Evolution statistics for 5000 randomly generated logical states. The GRAPE-optimized 134.6-ns control pulse (dark blue) leads to a 2.2% increase in average state fidelity, corresponding to a 81.3% reduction in average error, and a 67% reduction in standard deviation over linear ramping of the electrical parameters over the same duration (light blue).

B. ARBITRARY QUBIT STATE TRANSFER

In the context of a general quantum information processing sequence, the qubit state cannot be assumed to be an eigenstate. In this case, optimal control pulses do not significantly accelerate high-fidelity operating regime transfers; however, maximal fidelity is increased (see Fig. 4). In the case of completely unknown qubit states, simulated by applying the control pulses to logic states of the general form $|\psi\rangle = \alpha|0\rangle + \beta|1\rangle$, with α and β being randomly generated complex numbers according to Haar measure randomization [47], it is found that peak fidelity is always reached with 134.6-ns control pulses, showing that the operator approach to optimal pulse design yields state-agnostic controls (see Fig. 5), which is not the case, in general, for linearly ramped controls. When the optimal 134.6-ns control pulse is applied to a large number of randomly generated logic states, it is found that this approach designs a state-robust pulse, with high-fidelity low-variance operating regime transfers, which do not require a priori knowledge of the qubit's state (see Fig. 6). This is crucial for quantum computation applications, as the qubit's operating regime will need to be transferred several times during a computation, without having access to the qubit's state.

C. EFFECTIVE DECOHERENCE RATE

Astute readers might be surprised by the small amount of effective decoherence observed in the fidelity curves depicted in Figs. 2–5. Experimental results [21] have shown that despite charge relaxation and dephasing rates in the tens of megahertz, the total measured spin decoherence rate is as small as 2.4 MHz. The theoretical effective spin relaxation rate due to charge–phonon coupling was studied in [26] and shown to be equal to

$$\gamma_{1,s} = \gamma_{1,c}\left(\frac{2t_c}{\Omega}\right)\left[\frac{2t_c g\mu_B B_x}{(\Omega^2 - E_z^2)}\right]^2 + \mathcal{O}\left(B_x^4\right) \tag{26}$$

where $E_z = g\mu_B B_z$ is the Zeeman energy and $\gamma_{1,c}$ is the phonon-induced charge relaxation rate. Likewise, low-frequency charge fluctuations induce dephasing rates proportional to first- and second-order derivatives of the transition frequencies given by [26]

$$\gamma_{\phi,s}^{(1)} = \frac{\gamma_\phi|\epsilon|}{E_z}\left[\frac{2t_c g\mu_B B_x}{(\Omega^2 - E_z^2)}\right]^2 + \mathcal{O}\left(B_x^4\right) \tag{27}$$

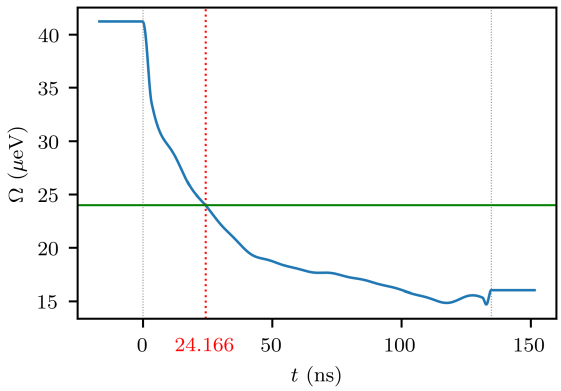

FIGURE 7. Orbital energy Ω throughout the optimal control sequence, which is applied between the vertical dotted gray lines. The horizontal green line shows the Zeeman energy, which does not change. The red dotted line indicates the time, at which the qubit orbital energy crosses this Zeeman energy threshold.

and

$$\gamma_{\phi,s}^{(2)} = \frac{\gamma_\phi^2}{E_z}\left[\frac{2t_c g\mu_B B_x}{\left(\Omega^2 - E_z^2\right)}\right]^2\left[1 - \frac{4\epsilon^2}{\Omega^2 - E_z^2}\right] + \mathcal{O}\left(B_x^4\right) \tag{28}$$

where γ_ϕ is the amplitude of the low-frequency charge fluctuations. Because $\Omega^2 - E_z^2$ appears in the denominator, it is easy to see from (26)–(28) that the total effective spin decoherence rate is expected to be very small relative to the total charge relaxation and dephasing rates except when the qubit orbital energy Ω and Zeeman splitting E_z are at resonance; this is illustrated in Figs. 7 and 8. Of course, crossing this resonance threshold is unavoidable given the chosen initial and final operating regimes. On the one hand, the memory-mode regime greatly benefits from a large energy detuning ϵ, which leads to a large orbital energy Ω. On the other hand, the flopping-mode regime benefits from small orbital energies in order to reduce charge relaxation rates (see Appendix A). Another set of controls has been generated for two operating regimes with orbital energies below the Zeeman threshold, such that the transient high-decoherence point when the orbital energy Ω crosses the Zeeman energy threshold is avoided. This is discussed further in Appendix B.

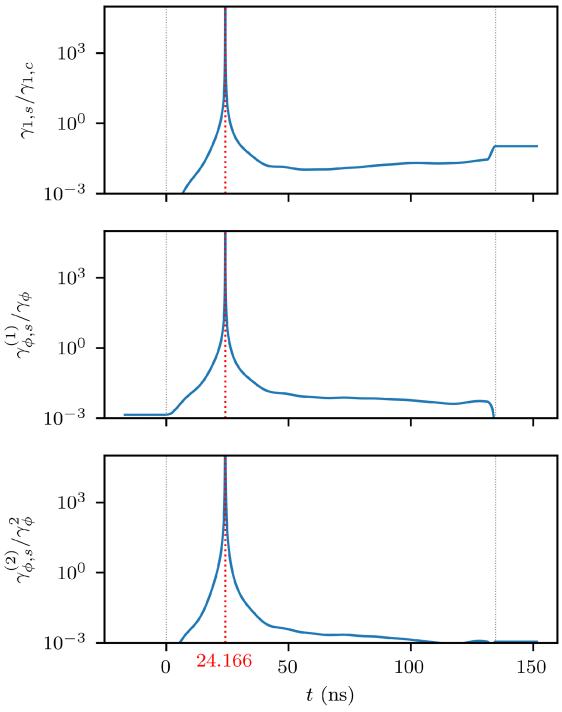

FIGURE 8. (Top) Effective phonon-induced spin relaxation and (middle and bottom) first- and second-order charge-induced spin dephasing rates during the optimal control pulse. The total effective spin decoherence rate is greatly increased when the qubit orbital energy Ω crosses the Zeeman splitting E_z, as indicated by the vertical dotted red line (see Fig. 7).

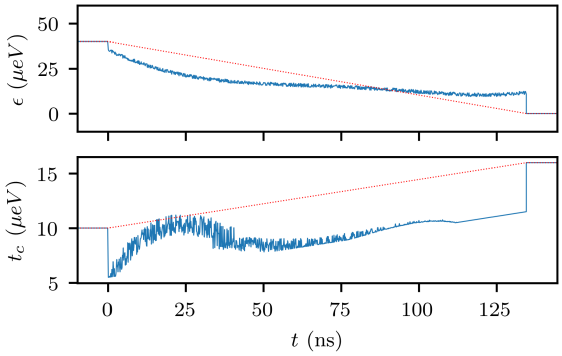

FIGURE 9. Optimal 134.6-ns control pulse generated by GRAPE for arbitrary state transfer. Electrostatic energies for $t < 0$ and $t > T$ correspond to the initial memory-mode and final flopping-mode configurations, respectively. The red dotted lines correspond to the naked adiabatic ramp controls; the difference between the two curves corresponds to the corrective term optimized by the GRAPE algorithm.

V. EXPERIMENTAL CONSIDERATIONS

The resulting optimal pulses used to transfer arbitrary qubit states from the memory-mode regime to the flopping-mode operating regime are shown in Fig. 9. As is common when using the GRAPE algorithm, the final pulses present two undesirable features, namely, high-frequency spectral content (up to tens of gigahertz) and sharp discontinuities at the beginning and at the end of the control. These features render experimental reproduction of these pulses very difficult even with modern arbitrary waveform generators, especially considering the low-pass filtering imposed by cryogenic control lines, despite previous successful implementations with these undesirable features of GRAPE-designed control pulses in experiments [36], [37], [38], [39]. The first of these features can be negated by using a simple low-pass filter on the optimal control pulses and observing the effects of a variable cutoff frequency on the resulting state fidelity, which are illustrated in Fig. 10. As shown, there is no appreciable degradation in the quality of the state transfer even for cutoff frequencies as low as 50 MHz,

IEEE Transactions on Quantum Engineering

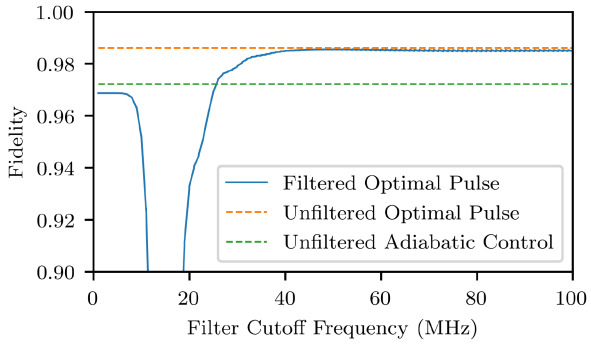

FIGURE 10. Operating regime transfer fidelity from the initial memory-mode to final flopping-mode configurations for qubit state $|0\rangle + |1\rangle$, as a function of the low-pass filter cutoff frequency applied to the control signal. As expected, the transfer fidelity attained by the filtered control pulse (solid blue line) approaches that of adiabatic ramping (green dotted line) for very low cutoff frequencies, whereas higher cutoff frequencies approach unfiltered optimal control performance (orange dotted line).

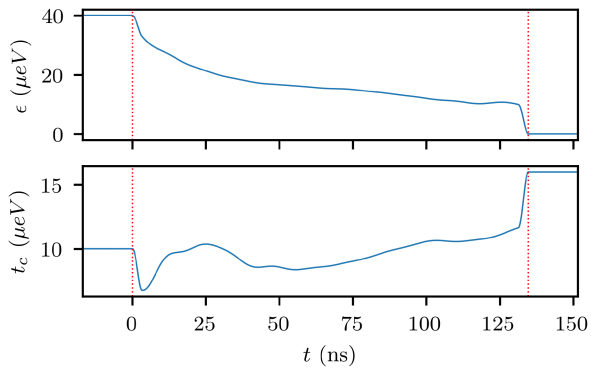

FIGURE 11. Filtered and windowed 134.6-ns control pulses. The optimal control pulse (see Fig. 9) was passed through an 80-MHz low-pass filter and windowed to eliminate discontinuities at the boundaries. The vertical lines correspond to $t = 0$ and $t = T$; electrostatic energies outside these bounds correspond to the initial memory-mode and final flopping-mode configurations, respectively.

much lower than the maximum bandwidth on high-frequency control lines of cryogenic apparatus. The second undesirable feature (sharp discontinuities) is removed by applying a Tukey window with a small α-factor (here $\alpha = 0.05$), effectively forcing initial and final control pulse amplitudes to the steady-state values for ϵ and t_c in the initial and final operating regimes, respectively. The resulting filtered and windowed control pulses are shown in Fig. 11. Once again, this experimentally feasible version of the optimal control pulses has been applied in simulation to randomly generated logical states of the general form $|\psi\rangle = \alpha\,|0\rangle + \beta\,|1\rangle$, with α and β being randomly generated complex numbers according to Haar measure randomization [47]. This experimentally feasible version shows virtually no loss of fidelity from the low-pass filtering and windowing of the control signals (see Fig. 12).

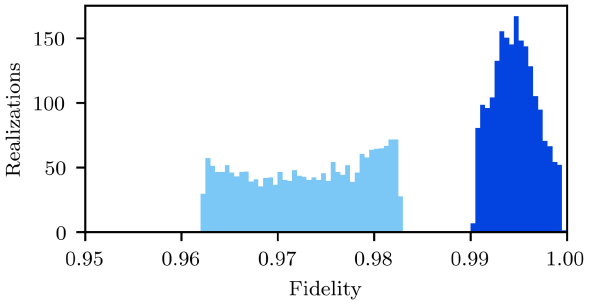

FIGURE 12. Evolution statistics for 5000 randomly generated logical states, using the filtered and windowed signals shown in Fig. 11. The filtering and windowing operations lead to no significant decrease in control performance when compared to the results shown in Fig. 6.

VI. CONCLUSION

In this article, it was shown that an algorithmic approach based on GRAPE to designing control pulses by iterating toward a target operator rather than a target state leads to state-robust and state-agnostic control pulses for DQD operating regime transfers. When the qubit is prepared in a known Hamiltonian eigenstate, the operating regime transfer can be executed significantly faster than with a standard adiabatic pulse while reaching fidelities greater than 99%. When the qubit is prepared in any other arbitrary state, optimal control pulses, which have been filtered and windowed for experimental feasibility, reach fidelities greater than 99% without a priori knowledge of the qubit state, which was not possible using linear ramping of the electrical parameters.

Building a universal quantum computer remains an outstanding challenge, yet the application of optimal control methods to the specific needs of a given qubit architecture is a critical part of development that lies between fundamental physics research and engineering for the operation of large-scale quantum processors.

APPENDIX A
CHARGE RELAXATION RATE

The rate of charge relaxation via emission of LA phonons in a steady-state regime can be obtained by writing the charge–phonon interaction Hamiltonian and using Fermi's golden rule at 0 K, yielding [20]

$$\gamma_{1,c} = \frac{2\pi}{\hbar}\sum_{\vec{k}} |c_{\vec{k}}|^2 \delta(\Omega - E_f) = \frac{2\pi}{\hbar}|c_k|^2 D(\Omega) \tag{29}$$

with phonon energy E_f. This equation shows an implicit dependence of the charge relaxation rate on the orbital energy Ω, which we now make explicit by using the Debye model for the phonon density of states [48]

$$D(\Omega) = \frac{V\Omega^2}{2\pi^2\hbar^2 v_s^3} \tag{30}$$

and the expression for the coefficient c_k [49]

$$|c_k|^2 = \frac{d^2}{2\rho v_s^2 V}\hbar v_s k. \tag{31}$$

In (30) and (31), d is the deformation potential, V is the device volume, Ω is the orbital energy, v_s is the speed of sound in the crystal, ρ is the crystal density, and k is the wave vector modulus. Using the dispersion relation

$$k = \frac{2\pi}{\lambda} = \frac{\Omega}{\hbar v_s} \tag{32}$$

the charge relaxation rate can be written in energy units as

$$\gamma_{1,c} = \frac{1}{2\pi\hbar^3}\frac{\Omega^3 d^2}{\rho v_s^5}. \tag{33}$$

It is, thus, seen that the charge relaxation rate via emission of LA phonons has cubic dependence on the orbital energy of the qubit and, therefore, depends on the amplitude of the control voltages applied to the gates. Using $d = 8.89$ eV, $\rho = 2330$ kg/m^3, and $v_s = 8433$ m/s^2 for silicon [50], [51], [52], (33) yields charge relaxation rates, which are consistent with experimental measurements found in the literature [21].

However, in the context of controlling the operating regime of the DQD, charge relaxation via emission of LA phonons in the silicon lattice is dependent on the control amplitudes ϵ and t_c via the electron orbital energy $\Omega \equiv \Omega(\epsilon, t_c)$. Attempting to optimize the control signals on ϵ and t_c while taking the exact dependence of this relaxation process on $\Omega(\epsilon, t_c)$ leads to transcendental equations, which are extremely computationally expensive to solve, for a very small projected gain in precision given the short duration of the control sequence relative to the decoherence rates involved. Instead, constant rates chosen to represent the worst case given the dynamic range for parameters ϵ and t_c are used in simulation.

APPENDIX B
ALTERNATIVE LOW-ENERGY OPERATING REGIMES

To evaluate the impact of the Zeeman threshold crossing on the performance of the optimal control pulse discussed previously in Section IV-C, another control sequence has been generated using a low-energy memory-mode regime, with $\epsilon = 20$ μeV (as opposed to $\epsilon = 40$ μeV), and all other parameters kept unchanged ($t_c = 10$ μeV, $B_x = 1.62$ μeV, and $B_z = 24$ μeV).

In this case, the optimal control duration was found to be 130.9 ns. The optimal filtered and windowed control pulses are illustrated in Fig. 13, and resulting evolution statistics for randomly generated logical states (see Fig. 14) show an appreciable gain in transfer fidelity when avoiding the Zeeman energy threshold. The quantitative improvements obtained from using this low-energy memory-mode regime are indicated in Table 1, showing most importantly a 66.15% reduction in average fidelity error and a 71.11% reduction in standard deviation relative to the results for the default high-detuning memory mode. Note, however, that this gain might be offset by a reduced quality in the memory-mode regime as the smaller energy detuning ϵ reduces the degree to which the spin state is protected from environmental noise. It seems likely that the preferred default memory-mode configuration would be the higher detuning regime used in the main body of this article, although this alternative low-energy configuration might be preferred in the course of a more complex multistep protocol running on this architecture. The choice of which operating regime to use should be made based on the specific needs of the application.

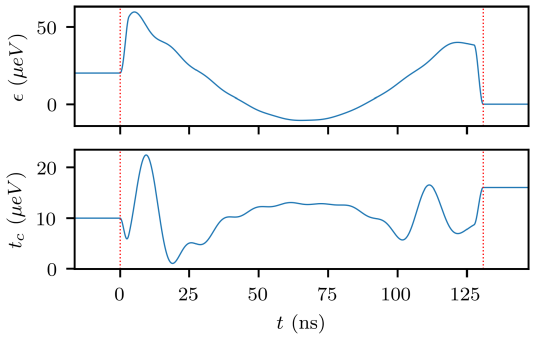

FIGURE 13. Filtered and windowed 130.9-ns control pulses. The optimal control pulse was passed through the same 80-MHz low-pass filter and windowed to eliminate discontinuities at the boundaries, similarly to the treatment applied to the pulse described in Section IV. The vertical lines correspond to $t = 0$ and $t = T$; electrostatic energies outside these bounds correspond to the initial low-energy memory-mode and final flopping-mode configurations, respectively.

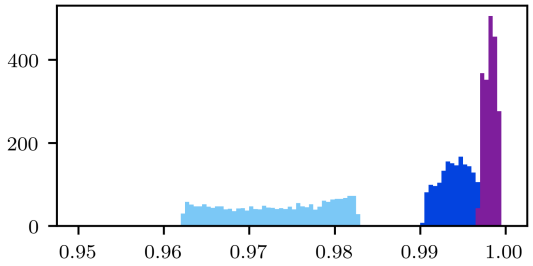

FIGURE 14. Evolution statistics for 5000 randomly generated logical states, using the filtered and windowed signals shown in Fig. 13, in purple. Previous results for the high-detuning memory-mode regime were reproduced for reference, using the filtered optimal control signal (dark blue) and adiabatic ramp control (light blue). Using low-energy configurations to avoid the Zeeman energy threshold results in a further improvement in transfer fidelity.

TABLE 1. Statistical Analysis of Evolution Results for Each Control Scheme

Fidelity Quantity	Optimal Control		Reference
	Low-Energy Memory Mode	Default Memory Mode	Adiabatic Ramp
Average	0.998182	0.994728	0.973552
Maximum	0.999386	0.999509	0.982720
Minimum	0.996911	0.990442	0.962314
Median	0.998235	0.994613	0.973634
Standard deviation	0.000667	0.002585	0.005825

APPENDIX C
OVERVIEW OF THE GRAPE ALGORITHM

The GRAPE algorithm, initially developed for nuclear magnetic resonance spectroscopy and detailed in [35], has become one of the most widely used optimal control algorithms in applications dealing with quantum systems. This appendix

IEEE Transactions on Quantum Engineering

is meant to provide the reader with a brief summary of the algorithm and the theory behind the method; readers interested in more details or motivations behind the development of this algorithm should refer back to the original paper.

Consider the state of a spin system, described by the density operator $\rho(t)$ and its equation of motion

$$\dot{\rho}(t) = -i\left[\left(H_0 + \sum_{k=1}^{m} u_k(t)H_k\right), \rho(t)\right] \tag{34}$$

where H_0 is the free evolution Hamiltonian of the system and H_k are the control Hamiltonians for each control field with amplitudes $u_k(t)$. The goal is to find the set of optimal control amplitudes for these control fields such that the state of the system is steered from an initial state $\rho(0) = \rho_0$ to some target state $\rho(T)$ in some specified time T; the figure of merit ϕ_0 to be optimized is the overlap between this final density operator $\rho(T)$ and the target density operator C, as measured by the inner product

$$\phi_0 = \langle C|\rho(T)\rangle = \mathrm{Tr}\{C^\dagger \rho(T)\}. \tag{35}$$

The GRAPE algorithm discretizes the total control time T into N time intervals of equal duration $\Delta t = T/N$. During a given time interval, the amplitude of each control field $u_k(j)$ is kept constant, leading to the time-evolution operator during the jth interval given by

$$U_j = \exp\left\{-i\Delta t\left(H_0 + \sum_{k=1}^{m} u_k(j)H_k\right)\right\}. \tag{36}$$

Optimizing ϕ_0 requires a measure of how the operator fidelity changes with perturbations to the control amplitude $\delta u_k(j)$. When Δt is small, we find to first order in Δt

$$\frac{\delta\phi_0}{\delta u_k(j)} = -\langle \lambda_j | i\Delta t\left[H_k, \rho_j\right]\rangle \tag{37}$$

where ρ_j is the density operator for the system during the jth time interval, and λ_j is the backpropagated target density operator C in the same time interval. Therefore, ϕ_0 is increased if the controls are varied in the direction of the gradient, that is, if we choose at each iteration

$$u_k(j) \to u_k(j) + \epsilon\frac{\delta\phi_0}{\delta u_k(j)} \tag{38}$$

where ϵ is a small step size. Therefore, the GRAPE algorithm iterative loop is as follows: starting from some initial set of guess controls $u_k(j)$ (either chosen randomly or set by an educated guess), compute ρ_j and λ_j from the initial state ρ_0 and target state C, respectively, for all $j \leq N$. These quantities are then used to update the control amplitudes $u_k(j)$ according to (38). The algorithm terminates when the fidelity ϕ_0 does not change by more than some termination threshold. Note that execution of the GRAPE algorithm requires only two full time evolutions per iteration (one forward for $\rho(t)$ and one backward for C), as opposed to conventional approaches, which usually require one full time evolution per parameter in the control space, leading to an optimization that is orders of magnitude faster [35].

Similarly, the GRAPE algorithm can be used to synthesize a unitary operator (rather than steer a system toward a particular state), as was done in the main body of this work. To achieve this, the initial density operator ρ_0 is set to the identity, and the target operator C is set to the unitary to be synthesized, rather than the target state in the initial formulation. There are some mathematical particularities that arise when using GRAPE in this manner, which are discussed in detail in [35].

REFERENCES

[1] D. Loss and D. P. DiVincenzo, "Quantum computation with quantum dots," *Phys. Rev. A*, vol. 57, 1998, Art. no. 120, doi: 10.1103/PhysRevA.57.120.

[2] G. Burkard, H.-A. Engel, and D. Loss, "Spintronics and quantum dots for quantum computing and quantum communication," *Fortschritte der Physik*, vol. 48, pp. 965–986, 2000, doi: 10.1002/1521-3978(200009)48:9/11<965::AID-PROP965>3.0.CO;2-V.

[3] R. Hanson, L. P. Kouwenhoven, J. R. Petta, S. Tarucha, and L. M. K. Vandersypen, "Spins in few-electron quantum dots," *Rev. Modern Phys.*, vol. 79, pp. 1217–1265, 2007, doi: 10.1103/RevModPhys.79.1217.

[4] A. R. Mills, D. M. Zajac, M. J. Gullans, F. J. Schupp, T. M. Hazard, and J. R. Petta, "Shuttling a single charge across a one-dimensional array of silicon quantum dots," *Nature Commun.*, vol. 10, 2019, Art. no. 1063, doi: 10.1038/s41467-019-08970-z.

[5] A. J. Sigillito, J. C. Loy, D. M. Zajac, M. J. Gullans, L. F. Edge, and J. R. Petta, "Site-selective quantum control in an isotopically enriched $^{28}Si/Si_{0.7}Ge_{0.7}$ quadruple quantum dot," *Phys. Rev. Appl.*, vol. 11, 2019, Art. no. 061006, doi: 10.1103/PhysRevApplied.11.061006.

[6] A. M. Tyryshkin et al., "Electron spin coherence exceeding seconds in high-purity silicon," *Nature Mater.*, vol. 11, pp. 143–147, 2012, doi: 10.1038/nmat3182.

[7] F. A. Zwanenburg et al., "Silicon quantum electronics," *Rev. Modern Phys.*, vol. 85, 2013, Art. no. 961, doi: 10.1103/RevModPhys.85.961.

[8] M. Veldhorst et al., "An addressable quantum dot qubit with fault-tolerant control-fidelity," *Nature Nanotechnol.*, vol. 9, pp. 981–985, 2014, doi: 10.1038/nnano.2014.216.

[9] A. J. Sigillito, M. J. Gullans, L. F. Edge, M. Borselli, and J. R. Petta, "Coherent transfer of quantum information in a silicon double quantum dot using resonant SWAP gates," *npj Quantum Inf.*, vol. 5, 2019, Art. no. 110, doi: 10.1038/s41534-019-0225-0.

[10] D. M. Zajac et al., "Resonantly driven CNOT gate for electron spins," *Science*, vol. 359, no. 6374, pp. 439–442, 2018, doi: 10.1126/science.aao5965.

[11] C. H. Yang et al., "Silicon qubit fidelities approaching incoherent noise limits via pulse engineering," *Nature Electron.*, vol. 2, pp. 151–158, 2019, doi: 10.1038/s41928-019-0234-1.

[12] T. Meunier, V. E. Calado, and L. M. K. Vandersypen, "Efficient controlled-phase gate for single-spin qubits in quantum dots," *Phys. Rev. B*, vol. 83, 2011, Art. no. 121403, doi: 10.1103/PhysRevB.83.121403.

[13] T. F. Watson et al., "A programmable two-qubit quantum processor in silicon," *Nature*, vol. 555, pp. 633–637, 2018, doi: 10.1038/nature25766.

[14] E. Chanrion et al., "Charge detection in an array of CMOS quantum dots," *Phys. Rev. Appl.*, vol. 14, 2020, Art. no. 024066, doi: 10.1103/PhysRevApplied.14.024066.

[15] P.-A. Mortemousque et al., "Coherent control of individual electron spins in a two dimensional array of quantum dots," *Nature Nanotechnol.*, vol. 16, pp. 296–301, 2021, doi: 10.1038/s41565-020-00816-w.

[16] N. W. Hendrickx et al., "A four-qubit germanium quantum processor," *Nature*, vol. 591, no. 7851, pp. 580–585, Mar. 2021, doi: 10.1038/s41586-021-03332-6.

[17] A. Blais, R.-S. Huang, A. Wallraff, S. M. Girvin, and R. J. Schoelkopf, "Cavity quantum electrodynamics for superconducting electrical circuits: An architecture for quantum computation," *Phys. Rev. A*, vol. 69, no. 6, Jun. 2004, Art. no. 062320, doi: 10.1103/PhysRevA.69.062320.

[18] A. Wallraff et al., "Strong coupling of a single photon to a superconducting qubit using circuit quantum electrodynamics," *Nature*, vol. 431, pp. 162–167, 2004, doi: 10.1038/nature02851.

[19] L. DiCarlo et al., "Demonstration of two-qubit algorithms with a superconducting quantum processor," *Nature*, vol. 460, pp. 240–244, 2009, doi: 10.1038/nature08121.

[20] M. Benito, X. Mi, J. M. Taylor, J. R. Petta, and G. Burkard, "Input-output theory for spin-photon coupling in Si double quantum dots," *Phys. Rev. B*, vol. 96, 2017, Art. no. 235434, doi: 10.1103/PhysRevB.96.235434.

[21] X M. Mi et al., "A coherent spin–photon interface in silicon," *Nature*, vol. 555, no. 7698, pp. 599–603, Mar. 2018, doi: 10.1038/nature25769.

[22] J. J. Viennot, M. C. Dartiailh, A. Cottet, and T. Kontos, "Coherent coupling of a single spin to microwave cavity photons," *Science*, vol. 349, no. 6246, pp. 408–411, 2015, doi: 10.1126/science.aaa3786.

[23] M. Pioro-Ladriére, Y. Tokura, T. Obata, T. Kubo, and S. Tarucha, "Micromagnets for coherent control of spin-charge qubit in lateral quantum dots," *Appl. Phys. Lett.*, vol. 90, 2007, Art. no. 024105, doi: 10.1063/1.2430906.

[24] J. Yoneda et al., "Robust micromagnet design for fast electrical manipulations of single spins in quantum dots," *Appl. Phys. Exp.*, vol. 8, 2015, Art. no. 084401, doi: 10.7567/APEX.8.084401.

[25] M. Benito et al., "Electric-field control and noise protection of the flopping-mode spin qubit," *Phys. Rev. B*, vol. 100, 2019, Art. no. 125430, doi: 10.1103/PhysRevB.100.125430.

[26] X. Croot et al., "Flopping-mode electric dipole spin resonance," *Phys. Rev. Res.*, vol. 2, 2020, Art. no. 012006, doi: 10.1103/PhysRevResearch.2.012006.

[27] E. Räsänen, A. Putaja, and Y. Mardoukhi, "Optimal control strategies for coupled quantum dots," *Open Phys.*, vol. 11, no. 9, pp. 1066–1073, 2013, doi: 10.2478/s11534-013-0277-2.

[28] F. Dolde et al., "High-fidelity spin entanglement using optimal control," *Nature Commun.*, vol. 5, no. 1, Feb. 2014, Art. no. 3371, doi: 10.1038/ncomms4371.

[29] L. K. Castelano, E. F. de Lima, J. R. Madureira, M. H. Degani, and M. Z. Maialle, "Optimal control of universal quantum gates in a double quantum dot," *Phys. Rev. B*, vol. 97, no. 23, Jun. 2018, Art. no. 235301, doi: 10.1103/PhysRevB.97.235301.

[30] D. S. A. Coden, S. S. Gomez, R. H. Romero, O. Osenda, and A. Ferrón, "Fast optical control of a coded qubit in a triple quantum dot," *Phys. Scripta*, vol. 94, no. 2, Jan. 2019, Art. no. 025101, doi: 10.1088/1402-4896/aaf763.

[31] F. A. Calderon-Vargas, E. Barnes, and S. E. Economou, "Fast high-fidelity single-qubit gates for flip-flop qubits in silicon," *Phys. Rev. B*, vol. 106, no. 16, Oct. 2022, Art. no. 165302, doi: 10.1103/PhysRevB.106.165302.

[32] A. Castro, A. G. Carrizo, S. Roca, D. Zueco, and F. Luis, "Optimal control of molecular spin qudits," *Phys. Rev. Appl.*, vol. 17, no. 6, Jun. 2022, Art. no. 064028, doi: 10.1103/PhysRevApplied.17.064028.

[33] F. L. Andreas et al., "Optimal control of a nitrogen-vacancy spin ensemble in diamond for sensing in the pulsed domain," *Phys. Rev. B*, vol. 106, no. 1, Jul. 2022, Art. no. 014202, doi: 10.1103/PhysRevB.106.014202.

[34] J. Yang, S. Pang, Z. Chen, A. N. Jordan, and A. del Campo, "Variational principle for optimal quantum controls in quantum metrology," *Phys. Rev. Lett.*, vol. 128, no. 16, Apr. 2022, Art. no. 160505, doi: 10.1103/PhysRevLett.128.160505.

[35] N. Khaneja, T. Reiss, C. Kehlet, T. Schulte-Herbrüggen, and S. J. Glaser, "Optimal control of coupled spin dynamics: Design of NMR pulse sequences by gradient ascent algorithms," *J. Magn. Reson.*, vol. 172, pp. 296–305, 2005, doi: 10.1016/j.jmr.2004.11.004.

[36] M. Nimbalkar et al., "Multiple-spin coherence transfer in linear Ising spin chains and beyond: Numerically optimized pulses and experiments," *Phys. Rev. A*, vol. 85, 2012, Art. no. 012325, doi: 10.1103/PhysRevA.85.012325.

[37] P. Groszkowski, A. G. Fowler, F. Motzoi, and F. K. Wilhelm, "Tunable coupling between three qubits as a building block for a superconducting quantum computer," *Phys. Rev. B*, vol. 84, no. 14, Art. no. 144516, Oct. 2011, doi: 10.1103/PhysRevB.84.144516.

[38] X.-D. Yang et al., "Assessing three closed-loop learning algorithms by searching for high-quality quantum control pulses," *Phys. Rev. A*, vol. 102, 2020, Art. no. 062605, doi: 10.1103/PhysRevA.102.062605.

[39] Z. Zong et al., "Optimization of a controlled- Z gate with data-driven gradient-ascent pulse engineering in a superconducting-qubit system," *Phys. Rev. Appl.*, vol. 15, no. 6, Jun. 2021, Art. no. 064005, doi: 10.1103/PhysRevApplied.15.064005.

[40] E. H. Chen et al., "Detuning axis pulsed spectroscopy of valley-orbital states in Si/SiGe quantum dots," *Phys. Rev. Appl.*, vol. 15, 2021, Art. no. 044033, doi: 10.1103/PhysRevApplied.15.044033.

[41] R. R. Hayes et al., "Lifetime measurements (T1) of electron spins in Si/SiGe quantum dots," 2009, *arXiv:0908.0173*, doi: 10.48550/arXiv.0908.0173.

[42] V. C. Lucy et al., "Hyperfine interactions in silicon quantum dots," *Phys. Rev. B*, vol. 83, no. 16, Apr. 2011, Art. no. 165301, doi: 10.1103/PhysRevB.83.165301.

[43] E. J. Connors, J. Nelson, L. F. Edge, and J. M. Nichol, "Charge-noise spectroscopy of Si/SiGe quantum dots via dynamically-decoupled exchange oscillations," *Nature Commun.*, vol. 13, no. 1, Feb. 2022, Art. no. 940, doi: 10.1038/s41467-022-28519-x.

[44] D. Manzano, "A short introduction to the Lindblad master equation," *AIP Adv.*, vol. 10, no. 2, 2020, Art. no. 025106, doi: 10.1063/1.5115323.

[45] H. P. Breuer and F. Petruccione, *The Theory of Open Quantum Systems*. London, U.K.: Oxford Univ. Press, 2002, doi: 10.1093/acprof:oso/9780199213900.001.0001.

[46] D. C. Lay, S. R. Lay, and J. J. MacDonald, *Linear Algebra and Its Applications*. 5th ed. London, U.K.: Pearson, 2014 [Online].Available: https://www.pearson.com/en-us/subject-catalog/p/linear-algebra-and-its-applications/P200000006235

[47] O. Di Matteo, "Understanding the Haar measure," Feb. 2021. [Online]. Available: https://pennylane.ai/qml/demos/tutorial_haar_measure/

[48] C. Kittel, *Introduction to Solid State Physics*, 8th ed. Hoboken, NJ, USA: Wiley, 2004 [Online]. Available: https://www.wiley.com/en-us/Introduction+to+Solid+State+Physics%2C+8th+Edition-p-9780471415268

[49] P. Zhao and D. Woolard, "Electron-longitudinal-acoustic-phonon scattering in double-quantum-dot based quantum gates," *Phys. Lett. A*, vol. 372, pp. 1666–1670, 2008, doi: 10.1016/j.physleta.2007.10.013.

[50] J. Witzens, "Ab initio calculation of the deformation potential and photoelastic coefficients of silicon with a non-uniform finite-difference solver based on the local density approximation," *Comput. Phys. Commun.*, vol. 185, pp. 2221–2231, 2014, doi: 10.1016/j.cpc.2014.03.016.

[51] L. J. Sham, "A calculation of deformation potentials in silicon," *Proc. Phys. Soc.*, vol. 81, no. 5, May 1963, Art. no. 934, doi: 10.1088/0370-1328/81/5/318.

[52] M. A. Hopcroft, W. D. Nix, and T. W. Kenny, "What is the Young's modulus of silicon?," *J. Microelectromech. Syst.*, vol. 19, no. 2, pp. 229–238, Apr. 2010, doi: 10.1109/JMEMS.2009.2039697.

V. Reiher received the B.Eng. and M.Sc.A. degrees in electrical engineering from Université de Sherbrooke, Sherbrooke, QC, Canada, in 2017 and 2021, respectively. He is currently working toward the Ph.D. degree in quantum engineering with the Institut Quantique, Université de Sherbrooke.

His research interests include optimal control of quantum systems, signal processing, and embedded system engineering.

Y. Bérubé-Lauzière received the Ph.D. degree in computer vision and image processing from McGill University, Montreal, QC, Canada, in 2002.

He is an Engineer and Physicist. Since 2003, he has been a Professor of electrical and computer engineering with the Université de Sherbrooke (UdeS), Sherbrooke, QC, where he is also a Researcher with the Institut Quantique. He was the Head of the Biophotonics Group, Institut National d'Optique, Québec City, QC. At UdeS, he was the Academic Director of the Electrical Engineering Bachelor's Degree Program from 2012 to 2015. Since 2018, he has been the Director of the NSERC-CREATE-Funded QSciTech Training Program that he set up. QSciTech provides added-value training in engineering design, project management, teamwork, intellectual property, and entrepreneurship to research students in quantum technologies to better prepare them for professional career. His research interests include optimal and feedback control of quantum systems, inverse problems, image reconstruction and instrumentation for diffuse optical tomography, and X-ray computed tomography.

Dr. Bérubé-Lauzière is a Professional Engineer in Canada.